Research Article

optica

Cubic meter volume optical coherence tomography: supplementary material

ZHAO WANG,[1] BENJAMIN POTSAID,[1,2] LONG CHEN,[3] CHRIS DOERR,[3] HSIANG-CHIEH LEE,[1] TORBEN NIELSON,[3] VIJAYSEKHAR JAYARAMAN,[4] ALEX E. CABLE,[2] ERIC SWANSON,[1,3] JAMES G. FUJIMOTO,[1,*]

[1]*Department of Electrical Engineering & Computer Science and Research Laboratory of Electronics, Massachusetts Institute of Technology, Cambridge MA, USA*
[2]*Advanced Imaging Group, Thorlabs Inc., Newton NJ, USA*
[3]*Acacia Communications Inc., Maynard, MA, USA*
[4]*Praevium Research Inc., Santa Barbara CA, USA*
**Corresponding author: jgfuji@mit.edu*

Published XX Month XXXX

This document provides supplementary information to "Cubic meter volume optical coherence tomography". The supplement provides more detailed information about the VCSEL laser, OCT imaging system, signal processing methods, additional details about the RF distortion correction and IQ correction, further evidence on the robustness of the distance measurement against laser drifts, methods to correct geometric distortions from the post-objective scanning, and an additional imaging example illustrating non-destructive evaluation of objects.

http://dx.doi.org/10.1364/optica.99.099999.s1 [supplementary document doi]

1. Laser configuration and characteristics

The VCSEL design was similar to that described in a previously published paper [1], which had a wide-gain, bandgap-engineered aluminum indium gallium arsenide (AlInGaAs) multi-quantum well active region epitaxially grown on an indium phosphide (InP) substrate and was joined by wafer bonding to a wideband bottom gallium arsenide based fully oxidized aluminum oxide (AlxOy)-GaAs bottom mirror. The cavity had a suspended top dielectric mirror separated from the underlying half-VCSEL structure by an air gap, which can be varied using electrostatic force through applied voltage to generate tunable emission. The electrostatic actuator used in the MEMS tuning structure is inherently nonlinear since the suspended mirror displacement varies as the square of the applied voltage. The VCSEL was optically pumped with a commercial wavelength stabilized laser (Innovative Photonic Solutions) at 976 nm through an isolator and the top dielectric mirror using a fiber optic wavelength division multiplexor (WDM). The WDM also separated the 1310 nm emission from the VCSEL which was then coupled to a semiconductor booster optical amplifier (Thorlabs BOA1130S) through a 1310 nm isolator. A polarization controller before the BOA was used to align the polarization of the VCSEL emission to match the polarization of the BOA with maximum gain.

In this study, the MEMS actuator was driven by an arbitrary voltage waveform synthesized by a function generator (Tektronix AFG 3102) and amplified with a 50x gain voltage amplifier (Trek 2100HF). The 100kHz repetition rate drive waveform from the function generator was shaped to achieve a quasi-linear sweep in wavenumber by adjusting 15 spline control points defining the waveform manually and subjectively evaluating the spacing of zero crossings from an auxiliary reference MZI set to a shallow delay. After a suitable waveform was found, it was stored in the arbitrary waveform generator and used for all imaging experiments. For imaging, residual non-linearity in k-space and sweep-to-sweep variation of the MEMS tuning trajectory were compensated using the calibration MZI shown in Fig. S1c. The BOA was modulated by the same function generator to amplify only the forward sweep, which resulted in a duty cycle of 42% and ~40 mW average output power from the BOA.

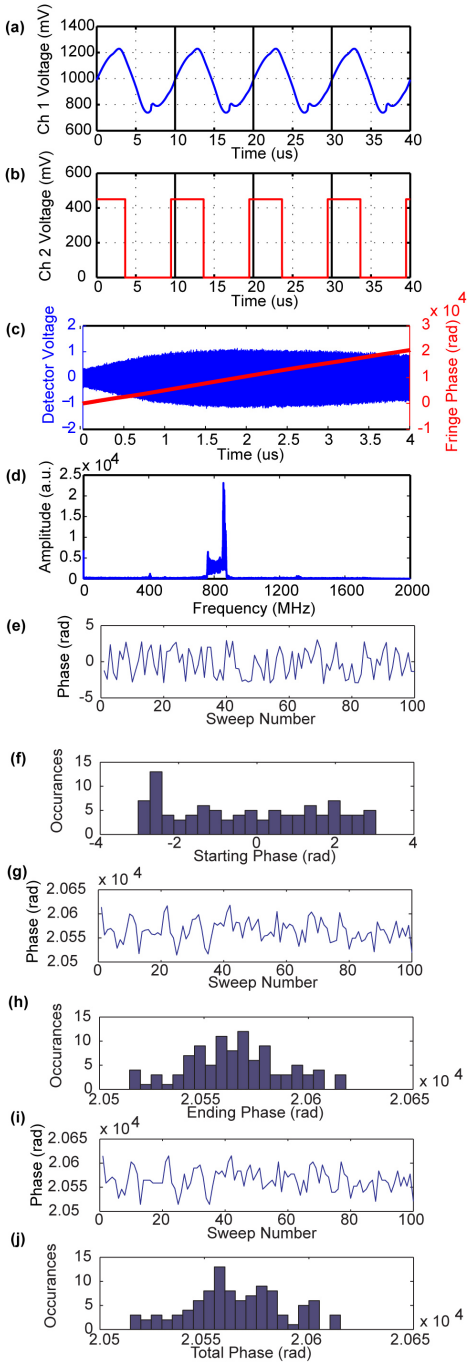

Fig. S1. Swept laser drive waveforms and sweep characteristics. (a) Arbitrary waveform generator signal for channel 1 (VCSEL). (b) Arbitrary waveform generator signal for channel 2 (BOA). Solid vertical black lines at 10 μs intervals indicate the position of the trigger signal from the arbitrary waveform generator. (c) Representative raw fringe from calibration MZI (blue) and the phase of the fringe (red) showing the high linearity of the sweep phase vs. time. (d) Direct FFT of Hann windowed fringe from (c) shows the small frequency variation and high linearity of the sweep. (e) MZI starting phase vs. sweep number. (f) Distribution of starting phase. (g) MZI ending phase vs. sweep number. (h) Distribution of ending phase. (i) MZI total accumulated phase vs sweep number. (j) Distribution of total phase.

Figure S1a shows the VCSEL drive waveform generated by the arbitrary waveform generator (channel 1). The channel 1 output was connected to a 50x voltage amplifier to drive the VCSEL. Fig. S1b shows the drive waveform for the BOA current driver as generated by the arbitrary waveform generator (channel 2). The waveform modulated the BOA on during the linear sweep and off during the sweep fly-back. Fig. S1c shows an example fringe from the calibration MZI (blue) as acquired within the 4 μs window of the oscilloscope acquisition and the fringe phase evolution curve (red) measured by a Hilbert transform. A high linearity in fringe phase vs. time is desirable to effectively use the A/D bandwidth and maximize the imaging range. Fig. S1d shows a Hann windowed fast Fourier transform of the raw fringe data shown in Fig. S1c. Sweep-to-sweep variations are present and the timing of the starting and ending MZI fringe phase can vary in the acquisition window. The starting fringe phase for 100 sequential sweeps measured by the calibration MZI is shown in Fig. S1e. The starting fringe phase corresponds to the start of the fringe phase vs. time curve (red line) in Fig. S1c and is evenly distributed between $-\pi$ and π, as shown in Fig. S1f. For the same 100 sequential sweeps, the ending fringe phase for each sweep is shown in Fig. S1g and Fig. S1h shows the phase distribution. Figs. S1i and S1j show the total accumulated fringe phase and the associated distribution. It is important to account for the sweep-to-sweep variation and resulting differences in accumulated phase in the data processing.

2. OCT imaging system

After the BOA, the output was directed to a 95:5 fiber optic coupler with 5% of the power used to monitor the emission with an optical spectrum analyzer (OSA) and the remaining 95% directed to a second 95:5 fiber optic coupler. From the second coupler, 95% was sent to the OCT interferometer and 5% to the calibration MZI. The OCT interferometer employed a dual circulator design. Light was split into sample (80%) and reference paths (20%) by a fiber optic coupler. Return light from the sample and reference path was directed by circulators to the sample (R) and local oscillator (L) inputs of the PIC receiver. The L receiver input had a polarization maintaining (PM) fiber. A polarization controller was used to align the reference arm light polarization to the PM fiber slow axis. Another polarization controller in the sample path was used to maximize the I and Q signal outputs from one of the polarization channels to improve detection efficiency. The output signals from the PIC receiver were digitized by an oscilloscope (DSA72004C, Tektronix Inc.) on channels 2 and 3 at 50 GS/s with 8 bit A/D converter resolution. The calibration MZI had an air gap mismatch of 3.6 cm between the two arms which generated a ~825 MHz beat frequency. The calibration MZI signal was detected by a 1.6 GHz bandwidth balanced receiver (Thorlabs PDB480C-AC) with output connected to the oscilloscope channel 1. The signal output from the integrated receiver and the MZI calibration signal were simultaneously acquired at 50 GS/s sample rate, resulting in 200,000 samples per wavelength sweep. The oscilloscope gains were set to optimize digitization of the sample interferograms and calibration MZI and were 50 mV/div for channel 1 and 10 mV/div for channels 2 and 3.

The oscilloscope had a relatively flat analog amplitude response up to 16 GHz and used digital DSP enhancement to extend the effective bandwidth to 18 GHz at the 10 mV/div gain setting. A B-scan of 1000 A-scans was acquired in 10 milliseconds. However, since the oscilloscope had limited memory (256 MB), data from only one B-scan with three channels could be acquired and had to be saved to disk before acquiring the next B-scan. A custom C++ program running on a host computer was used to control the oscilloscope for data acquisition via GPIB interface (National Instruments Corporation), and the acquired data were copied back to the host computer via Ethernet networking interface. The same program controlled the galvanometer scanners via the analog outputs of a data acquisition board (NI PCIe-6323, National

Instruments Corporation). The trigger signal from the function generator driving the VCSEL sweep was used to synchronize the laser sweep, galvanometer scanning, and data acquisition. A delay generator (Thurlby Thandar Instruments TGP 110) was used to adjust the sweep trigger timing to center the sweep within the oscilloscope acquisition window.

To measure repeatability, we used a flip mirror within the scanning subsystem that allowed the light from the 19 mm focal length lens to be directed to a fixed silver coated mirror mounted on a translation stage. Thus, the galvanometer scanners could be bypassed to obtain a measurement of a stationary sample.

The non-telecentric scanning generated non-uniform scanning area and varying sampling density as a function of distance from the scanners. The scale bar for each image example was based on the lateral scan dimension near the zero delay surface. For large objects (e.g. bicycle), the lateral dimension was sub-Nyquist sampled, especially for the parts of the object that were further away from the scanners. Better image quality can be achieved if a denser scan pattern were utilized.

3. Data processing

Figure S2 shows the signal processing algorithm used in this study. The raw interference spectra from the I and Q channels, and the MZI data were first up-sampled by a factor of two in the Fourier domain. The RF related phase distortion from the detection electronics was corrected in the Fourier domain using a polynomial function as described in the main text.

The phase evolution of the MZI fringe was obtained with a Hilbert transform as follows. The MZI signal was spectrally shaped using a Hann window, Fourier transformed, apodized in the Fourier domain with a 300 MHz bandwidth Hann spectral window centered around 825 MHz to extract the main components of the MZI signal while removing the DC and high frequency components. The phase of the filtered MZI signal was extracted by inverse Fourier transform, angle calculation, and phase unwrapping. The IQ data were resampled using the MZI phase by cubic spine interpolation. Sweep-to-sweep variation is cancelled in the interpolation step by selecting a subset of the data that corresponds to a fixed amount of accumulated MZI phase. For the data in this paper, only the region of IQ data corresponding to an MZI phase from 10 radians to 19600 radians was extracted and used. This range was determined by processing several data sets and noting the smallest experimental accumulated fringe phase. To account for edge effects related to the Hilbert transform and potential drift of the laser, the small signal at the edge of the sweep was discarded to obtain the 10 radians to 19,600 radian range. The interpolation step produces I and Q fringes that are both linear in wavenumber (k) and also corresponds to the predetermined and fixed accumulated phase range. The relative phase between the I and Q channels was further optimized using the method described in the main text and used to construct a complex signal. Background subtraction and spectral shaping were applied thereafter. In this study, we tried to match the reference and sample arm fiber length and air gap as closely as possible, and we found that the dispersion was well balanced between the two arms. However, if needed, a third order polynomial phase vector could be multiplied to the OCT spectrum to numerically compensate for residual dispersion imbalance. After FFT, the modulus of the data was logarithmically compressed for display.

3D rendering was performed using the software Amira (FEI, Oregon). The processed intensity volume (0.2 TB) was downsampled by 100 times in the axial dimension before volume rendering due to computer memory limitations. For the skull/brain data, both the axial and transversal geometric distortions due to non-telecentric scanning were corrected using the method described in Supplementary Note 7. Each volume was then segmented and surface reconstruction was generated for the four volumes. The non-skull/brain voxels were cropped out. The four reconstructed surfaces were manually aligned by rotating and translating individual object surfaces to generate a complete surface model (Visualization 3).

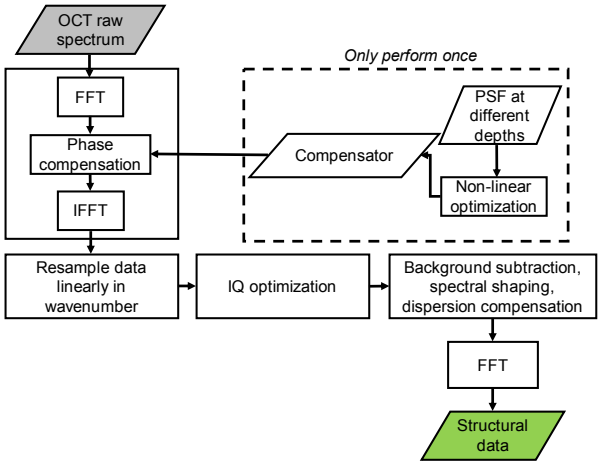

Fig. S2. Signal processing algorithm for meter-range OCT data.

4. RF phase calibration

Phase compensation of the detection electronics was shown to be critical for proper calibration of the OCT PSF at the high electrical frequencies associated with long distances. Fig. S3a and S3b show the magnitude and phase response of a normalized second order transfer function ($\omega_n = 1$ and $\zeta = 1$) representing a low pass filter. At low frequencies, the phase response is relatively flat. At moderate frequencies, the phase is relatively linear. However, approaching the cutoff frequency, the phase becomes non-linear. This phase behavior is typical of low pass filter designs. Although the exact order or characteristics of the low pass filters in the oscilloscope electronics are unknown, a non-linear phase behavior around the cut-off frequency is expected. Fig. S3c shows the phase correction obtained used for processing the data. The required phase correction is small at the low to mid frequencies and becomes larger approaching the cut-off frequency of the oscilloscope. Fig. S3d shows the FFT of the raw interferogram obtained from a silver coated mirror at distances of ~22 mm and ~719 mm. The interferogram at the closer distance 1 at ~22 mm has a narrow frequency bandwidth and resides in a linear region of the phase correction curve. The interferogram at the longer distance 8 at ~719 mm has a broad frequency bandwidth and resides in a highly non-linear region of the phase correction curve. It is clear that a simple time shift (application of a linear ramp in phase or equivalently, a correction to group delay) cannot compensate the phase errors and that a higher order correction is required.

Fig. S4a shows a comparison of sensitivity roll-off with and without phase correction. For the latter case, we optimized the group delay alone (time shift between sample and calibration MZI signals) without applying the full phase correction. Without phase correction, as shown in Fig. S4b-e, the PSF was acceptable at an imaging range of a few centimeters and significant side lobes appeared at mid ranges of 20-30 cm. Beyond 40 cm, the PSF was unusable, illustrating the importance of phase correcting the transfer function of the acquisition system.

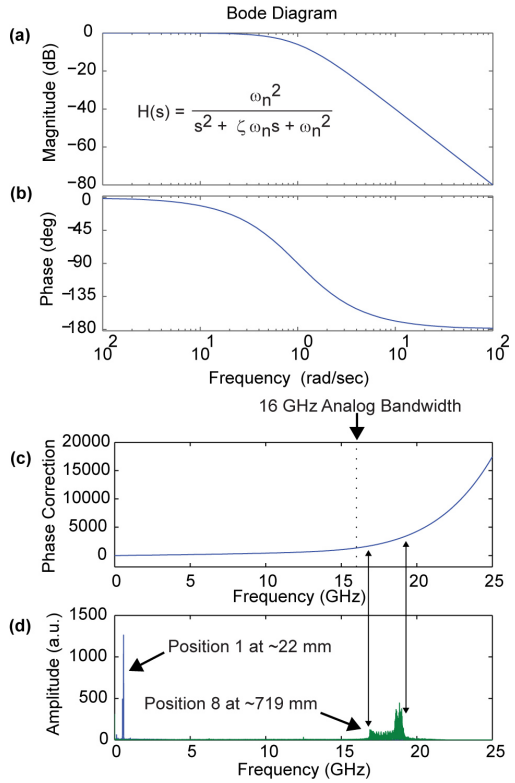

Fig. S3. Detection phase calibration. (a) Magnitude and (b) phase of a representative normalized second order transfer function with $\omega_n = 1$ and $\zeta = 1$. (c) Phase correction (blue) curve with the 16 GHz analog bandwidth of the oscilloscope indicated with the dashed vertical line (black). (d) Frequency content of raw and uncorrected fringes obtained from a silver coated mirror used as the sample at distances of ~22 mm and ~719 mm. Note that the phase correction was only fit over fringes ranging from distances 1 (~22mm) to 8 (~718mm) so data beyond the fitting regime above approximately 20GHz is extrapolated and may not represent the acquisition system phase.

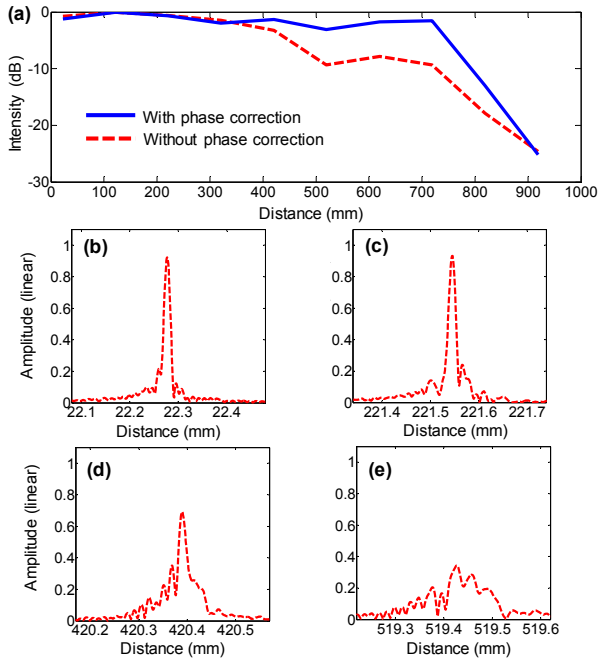

Fig. S4. Comparison of sensitivity roll-off with and without phase correction. (a) An ~8 dB sensitivity improvement at ranges >50 cm was achieved using phase correction. (b-e): Examples of PSFs without phase correction at four different depths, compared to with phase correction in Fig. 2d-i in the main text.

5. IQ correction

The IQ correction method presented in this paper did not change the SNR or dynamic range of the original signal (Fig. S5), and therefore the gain of the complex conjugate suppression was achieved without penalty. The limitation is that it did not correct potential RF dependent phase distortion between the IQ channels. However, it is likely that the mirror signal suppression obtained here was already approaching the hardware limit in this study, since a small pathlength mismatch or signal skew on a scale of 1-5 picoseconds between the two channels was sufficient to generate 10-25 dB deterioration in complex conjugate suppression with a 10 GHz fringe signal. For the oscilloscope used in this study, the time delay difference between any two channels is ≤10 ps according to the specifications. We aim to further optimize the PIC design in future studies to provide a more robust hardware solution for optimal IQ detection.

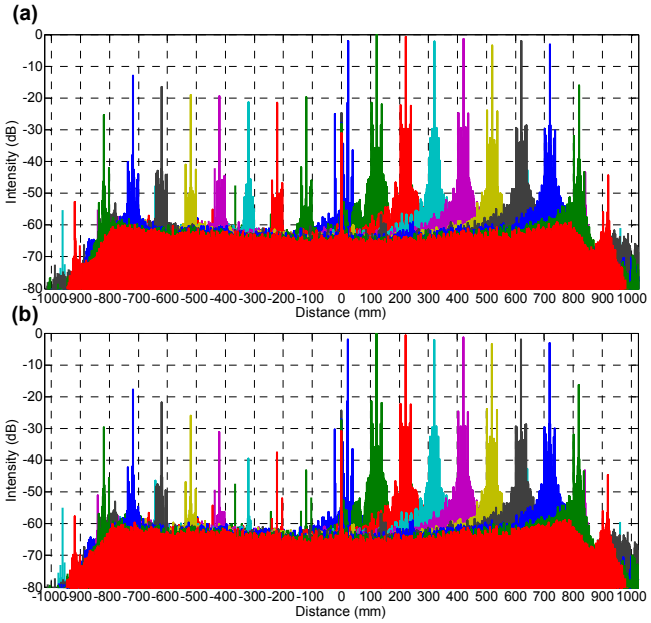

Fig. S5. Comparison of sensitivity roll-off and complex conjugate suppression before and after IQ phase correction. (a) Without IQ phase correction. (b) Using IQ phase correction.

6. Distance measurement precision is not affected by swept laser drift

In SS-OCT, there can be sweep-to-sweep variation or long-term drift of the swept laser. In the main text we showed that if a reference MZI is used to calibrate the OCT signal (see also Supplementary Note 3), the sweep variation does not affect the measurement precision. Modern SS-OCT systems are often employed with a k-clock to directly sample the data linearly in wavenumber. Although k-clocking was not used in our study because of the high sampling rate requirement, for the purpose of completing the theory, we further show that if a direct k-clock is available, measurement precision is also preserved in SS-OCT. Therefore, in practice, the measurement precision is only limited by environmental disturbances.

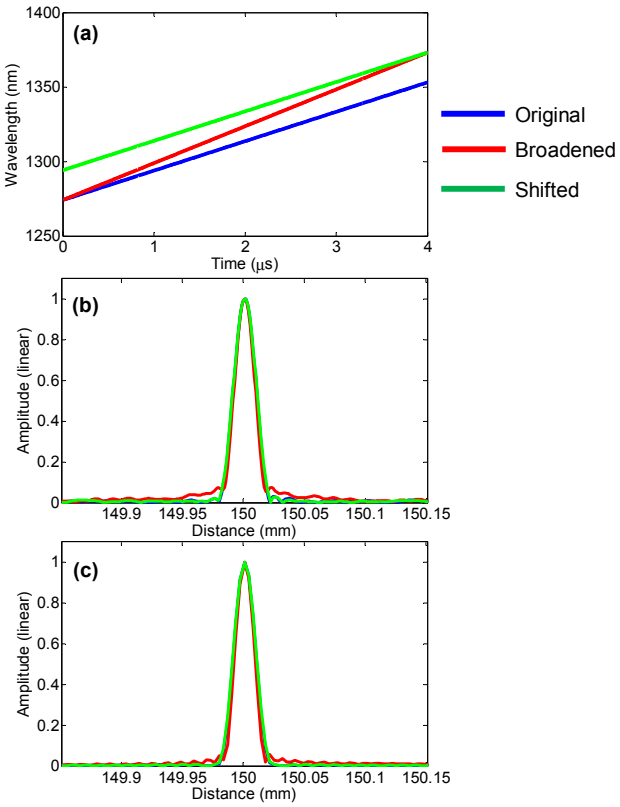

Fig. S6. Simulation of a mirror signal under different laser sweep conditions. (a) Blue: laser sweeps from 1274 nm to 1353 nm; Red: broadened laser sweeps from 1274 nm to 1373 nm; Green: shifted laser sweeps from 1294 nm to 1373 nm. (b) PSFs obtained with different laser sweep conditions by resampling the spectrum data using the calibration MZI. (c) PSFs obtained from direct Fourier transform of the simulated signal sampled using a k-clock. It should be noted that direct k-clock was not employed in this study.

When the OCT signal is directly sampled by an external k-clock [k_s], the axial scan can be generated by direct FFT. If the laser sweep range varies, the frequency of the OCT fringe signal vs. time will also fluctuate. However, the frequency of the k-clock and OCT fringe track each other because they are measured from the same laser sweep, making the fringe frequency vs. k invariant. Typically, the k-clock uses the zero-crossing points of an MZI to sample the data linearly in wavenumber. Using this method and neglecting the random phase terms because they do not affect the amplitude of the Fourier transformed data, *[k_s]* can be obtained as follows:

$$\begin{aligned} & E[k_s]_{MZI} = S(k_s)\left|E_1(k_s)\right|\left|E_2(k_s)\right|\cos(2k_s z_{12}) = 0 \\ & \Rightarrow 2k_s z_{12} = \frac{\pi}{2} + m\pi \\ & \Rightarrow k_s = \frac{\pi/2 + m\pi}{2z_{12}}, m = 0, \pm 1, \pm 2..., \end{aligned} \quad \textbf{(S1)}$$

Where *S(k)* is the power spectrum density of the laser, [k_s] is only dependent on z_{12}, which is the fixed air gap mismatch between the two arms of the MZI, and is independent of the laser sweep variation. Therefore, the frequency of the interference signal in k-space, or equivalently the sample position after Fourier transform is unchanged. This invariance is maintained as long as the k-clock frequency remains within the limits of the DAQ clock.

To further verify this hypothesis, we numerically simulated a mirror signal in SS-OCT under different laser sweep conditions (Fig. S6a): 1): laser sweeps 80 nm from 1274 nm to 1353 nm; 2): sweep range increased by 25% to 1274 nm -1373 nm; 3): sweep range shifted to 1294 nm -1273 nm. It should be noted that we used extreme conditions to demonstrate the robustness of the measurement, but such extreme variations rarely occur in practice if the swept laser is properly designed. The parameters used in the simulation were the same as in the imaging experiment: laser sweep repetition rate: 100 kHz (forward sweep only); duty cycle: 42%; data sampling rate: 50 GS/s; samples/A-scan: 200,000; sample mirror position: 150 mm. The MZI air gap was 3.6 cm for the case using MZI calibration. For k-clock, the MZI frequency was 2.7 times the maximum sample frequency. For MZI calibration, the data processing algorithm was the same as in Fig. S2, but no phase correction was needed. For k-clocking, the data resampling step was omitted and direct FFT was performed. Fig. S6b shows the PSFs after resampling the spectrum to be linear in wavenumber using a reference MZI under the three laser sweep conditions. The peak position of the PSFs, indicating the position of the sample, is constant regardless of the laser sweep variation. Fig. S6c shows the PSFs after Fourier transform of the spectrum directly sampled using a k-clock, and the peak position of the PSFs is also constant for all cases. This verifies the theory that OCT measurement precision is not affected by variations in the swept lasers.

7. Correcting geometric distortions

To achieve fast 2D scanning with a large scan area, we employed non-telecentric post objective scanning. This created geometric distortions in both the axial and transversal dimensions. Fig. S7 shows the scanning and image coordinate geometry. The scanning creates a nearly spherical imaging volume where the zero delay appears as a nearly spherical surface. For the purposes of this analysis, we assumed that the distance between the two galvanometer scanning mirrors was zero which would generate a spherical scan. However, the galvanometer mirrors were separated by a small distance which would cause the radii in the two scan directions to be slightly different. Since the scanner to object distance is large compared to the mirror separation, this is a small correction that we neglect in this analysis. A more detailed model could be used to fully correct for the scanner. Consider the flat (*en face*) object plane illustrated as the shaded area in Fig. S7. The center A-scan passing through point *O* has no geometric distortions. An arbitrary point *P* in the same object plane but from an oblique imaging angle has a different axial position with respect to the zero delay in the B-scan compared with point *O*. Further, they are related through the following equations:

$$\begin{aligned} PI &= PS - R \\ QS &= PS\cos(\theta) \\ OS &= QS\cos(\varphi) \\ OI' &= OS - R, \end{aligned} \quad \textbf{(S2)}$$

Where θ and φ are the scan angle of point *P* in the two lateral scanning directions X and Y, respectively; *R* is the radius of the sphere, or equivalently the absolute axial position of the reference mirror with respect to the scan center; *PI* and *OI'* are the original and corrected axial position with respect to the zero delay. In this example, we assume point *P* is further away than the reference mirror, but similar rules can be applied to the points that are closer than the zero delay. To verify the correction accuracy, we imaged a flat optical aluminum breadboard and applied the above correction method. Fig. S8b and S8c show the measured breadboard surface position before and after correction. Fig. S8d and S8e show a B-scan from the dotted line in Fig. S8a before and after correction. The distorted curved surface was corrected to a flat surface (Fig. S8f-g). The standard deviation of the corrected

surface position was 0.044 mm, which was less than the specified surface flatness of ±0.15 mm from the manufacturer (Thorlabs Inc.). Fig. S8h and S8i show the 3D rendering of the breadboard before and after correcting the axial distortions.

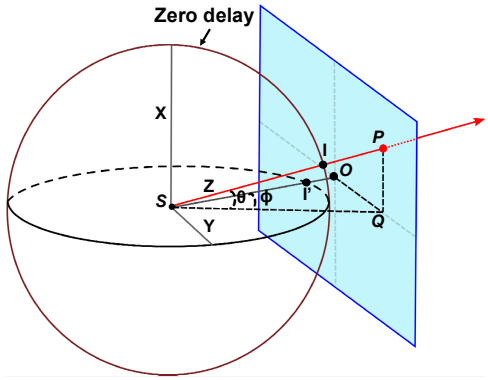

Fig. S7. Illustration of non-telecentric scanning geometry in meter-range OCT. Because the reference mirror position is fixed, the scanning mirror creates a quasi-spherical imaging volume where the zero delay plane appears as the surface of a sphere. *S*: scan center; *O*: intersection between the center beam and an orthogonal object plane; *P*: an arbitrary point on the same plane with an oblique incident angle; θ and φ: scanning angle in X and Y dimensions for point *P*, respectively; *I* and *I'*: axial position of the reference mirror.

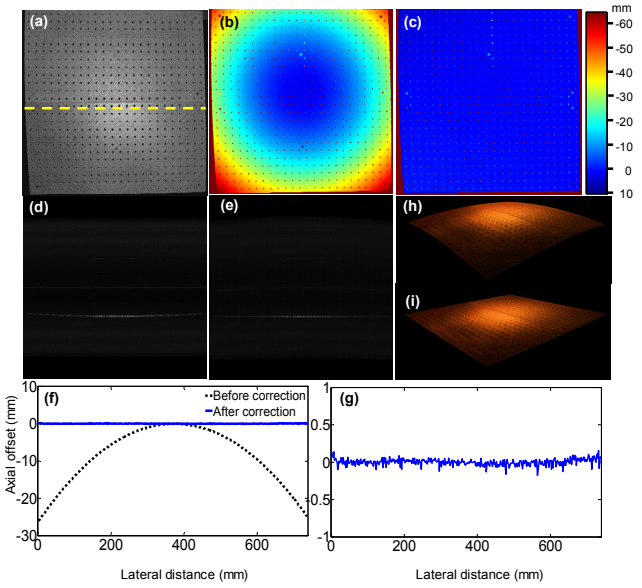

Fig. S8. Validation of axial dimensional distortion correction by imaging a flat aluminum breadboard. (a) *En face* projection of the OCT volumetric data. (b)–(c) Topological mapping of the breadboard surface before (b) and after correction (c). (d)-(e) Cross-sectional B-scans from the dotted line in (a) before (d) and after correction (e). (f) Plot of the breadboard surface position in (d-e) before and after correction. (g) Enlarged view of the breadboard surface after correction. (h)-(i) 3D visualization of the breadboard before (h) and after correction (i).

The lateral dimensional distortion correction is straightforward. The lengths of PQ and OQ characterize the lateral dimension of the *en face* object plane, and are proportional to the axial distance of point P from the scan center. We chose one arbitrary plane (e.g. center of the object) as the reference and corrected the lateral dimensions for the other *en face* planes in the volume.

8. Additional imaging examples

Meter-range OCT performs tomographic imaging, and can be used for non-destructive evaluation of internal structure in objects or transparent multilayered structures. Fig. S9 shows an example of imaging two-liter plastic bottles as a possible application in manufacturing quality control. The holes of the breadboard located far behind the bottles can be seen clearly, illustrating the capability to image multiple surfaces from a single A-scan.

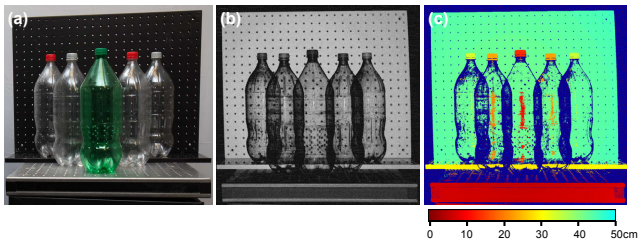

Fig. S9. Meter-range OCT imaging of two-liter plastic bottles for object inspection. The OCT volume has 1000x1000 A-scans. (a): Photograph. (b): Intensity projection of the OCT image. (c): Topological mapping of the objects.

References

1. Jayaraman, V. et al. High-speed ultra-broad tuning MEMS-VCSELs for imaging and spectroscopy. SPIE Microtechnologies; International Society for Optics and Photonics; 87630H-87630H (2013).